MOX–Report No. 41/2014

Impact of space-time mesh adaptation on solute transport modeling in porous media

Esfandiar, B.; Porta, G.; Perotto, S.; Guadagnini, A.

MOX, Dipartimento di Matematica "F. Brioschi"
Politecnico di Milano, Via Bonardi 9 - 20133 Milano (Italy)

lab-mox@polimi.it http://mox.polimi.it

Impact of space-time mesh adaptation on solute transport modeling in porous media

Bahman Esfandiar,[♯] Giovanni Porta,[♯] Simona Perotto,[♭] Alberto Guadagnini[♯,◇]

October 15, 2014

[♯] D.I.C.A., Politecnico di Milano, Italy
[♭] MOX, Dipartimento di Matematica, Politecnico di Milano, Italy
[◇] Dept. of Hydrology and Water Resources, University of Arizona, Arizona, USA
{bahman.esfandiar,giovanni.porta,simona.perotto,alberto.guadagnini}@polimi.it

Abstract

We implement a space-time grid adaptation procedure to efficiently improve the accuracy of numerical simulations of solute transport in porous media in the context of model parameter estimation. We focus on the Advection Dispersion Equation (ADE) for the interpretation of non-reactive transport experiments in laboratory-scale heterogeneous porous media. When compared to a numerical approximation based on a fixed space-time discretization, our approach is grounded on a joint automatic selection of the spatial grid and the time step to capture the main (space-time) system dynamics. Spatial mesh adaptation is driven by an anisotropic recovery-based error estimator which enables us to properly select the size, shape and orientation of the mesh elements. Adaptation of the time step is performed through an ad-hoc local reconstruction of the temporal derivative of the solution via a recovery-based approach. The impact of the proposed adaptation strategy on the capability to provide reliable estimates of the key parameters of an ADE model is assessed on the basis of experimental solute breakthrough data measured following tracer injection in a non-uniform porous system. Model calibration is performed in a Maximum Likelihood (ML) framework upon relying on the representation of the ADE solution through a generalized Polynomial Chaos Expansion (gPCE). Our results show that the proposed anisotropic space-time grid adaptation leads to ML parameter estimates and to model results of markedly improved quality when compared to classical inversion approaches based on a uniform space-time discretization.

1 Introduction

Transport of solute mass in the subsurface is due to advection and diffusion processes, taking place at the pore level. Due to practical difficulties to include

pore-scale modeling in the analysis of typical laboratory and field scale settings, solute transport in porous media is mostly described by means of effective models. Several alternative modeling options are available in this context. A standard choice is to adopt a continuum-based representation of the main governing processes grounded on the standard advection-dispersion equation (ADE). A key assumption underlying the ADE is that the total dispersion coefficient can be described by the sum of effective diffusion and hydrodynamic dispersion, according to the so-called Fickian analogy [1]. Limitations of this modeling option have been identified and discussed on the basis of theoretical arguments, numerical simulations and experimental evidences, which led to the development of alternative formulations encapsulating effective descriptions of non-Fickian (or anomalous) transport (see, e.g., [23, 29, 4, 57, 45] and references therein). These approaches encompass very different modeling perspectives, based on both Lagrangian and Eulerian mathematical formulations and can give rise to local and/or non-local (integro-differential) equations. All these macroscale models entail the definition of effective transport parameters, which are typically assumed to be linked to geometrical settings which are somehow representative of the pore space geometry. These parameters are generally unknown in laboratory and field scale applications, and need to be estimated by means of inverse modeling procedures. To this aim, multiple evaluations of the model of choice are typically required. While a considerable amount of analytical solutions is available [52], practical applications often require the use of methodologies based on numerical approximations of the governing equations to obtain the evolution of the concentration in the space-time domain of interest [1]. Independently of the approach employed, the results of numerical simulations are always subject to an approximation error, which is related to the selected discretization method. For instance, the computational error associated with Eulerian discretizations (e.g., finite elements, finite volumes, finite differences) is a function of the spatial grid spacing and of the time step size. This work is aimed at assessing the impact of the numerical discretization strategy on parameter estimation procedures, as applied to laboratory scale solute transport processes in porous media. To keep model complexity at a minimum level, we assume that transport can be modeled at a continuum scale by means of an ADE, which is solved in a finite element framework. We ground the numerical approximation of the ADE on a space-time adaptive discretization, following the methodology outlined in [14]. Here, we focus on the effect of this adaptive methodology on the quality of the estimates of dispersivity parameters associated with experimental solute breakthrough curves detected in a real heterogeneous porous system.

Previous studies show that the impact of discretization techniques on typical output variables of interest at reservoir/aquifer scales may be relevant [5, 22]. [39] show that the choice of the numerical methodology employed for the forward solution of transport problems can bear considerable effects on inverse modeling results. Automatic mesh and time step adaptation techniques provide a flexible tool to dynamically tie the resolution of the space-time mesh to the features of

the numerical solution of the target differential problem [31]. In the context of groundwater flow simulation, adaptive mesh methodologies have been applied to the simulation of free surface flows [27, 6], and to simulate flow in the presence of heterogeneous permeability fields [9, 33]. Adaptive mesh strategies have also been implemented for the simulation of transport processes in porous media, e.g., in [41, 42, 25, 21]. The majority of existing literature works rely on an isotropic local refinement of the spatial grid. A dynamic anisotropic mesh adaptation scheme is proposed in [51] for the simulation of reactive transport. The key advantage of anisotropic meshes is that they enable one to optimize the computational mesh in the presence of directional features of the solution of the mathematical model or of model outputs (e.g., concentration fronts induced by transport and/or reactive phenomena) when dealing with a goal-oriented approach [2].

Time-dependent behaviors characterize many relevant processes taking place in the subsurface. Recent studies show that an adaptive choice of the time step typically allows increasing the accuracy and efficiency of numerical solvers. For example, time step adaptation methodologies have been proposed for the simulation of density-driven flows [56], passive and reactive chemical transport [55, 47], and flow in variably saturated porous media [26].

Recent works demonstrate the effectiveness of combining anisotropic mesh and time step adaptations in the framework of, e.g., computational fluid dynamics [13, 35] and overland flow simulations [43, 44]. The methodology proposed in [43] has been recently applied by [14] to the simulation of solute transport in porous media. These authors compare the results obtained through the space-time adaptive methodology against experimental breakthrough curves measured at the outlet of a homogeneous sand box. The results of [14] indicate that (i) anisotropic mesh adaptation allows capturing early solute breakthrough, which is not reproduced as accurately by means of a fixed uniform space-time discretization, and (ii) time step adaptation allows reducing the computational cost, while preserving the accuracy of the results associated with the anisotropic mesh adaptation strategy.

The main objective of this work is to quantify the impact of the implementation of the space-time adaptive procedure proposed in [14] on parameter estimation and uncertainty quantification in the context of laboratory scale solute transport modeling. We ground our study on solute breakthrough curves measured at the outlet of a block-wise heterogeneous porous domain. To this end, we couple a space-time adaptive discretization with the model reduction technique proposed in [20]. The latter methodology provides a way to compute an approximation of the modeled breakthrough curve through a generalized polynomial chaos expansion (gPCE). The gPCE enables one to construct a surrogate model approximating a target system response through a finite series of polynomials. These are selected on the basis of the functional format of the probability density of the model uncertain parameters. The procedure allows performing multiple evaluations of the system model, which are employed to (a) obtain Maximum

Likelihood estimates of model parameters and (b) quantify propagation of parameter uncertainty to target model outputs at a reduced computational cost [15, 16, 11, 12]. The gPCE strategy can also lead to the analytical evaluation of the variance-based Sobol sensitivity indices [49, 50], which quantify the relative contribution of each uncertain model parameter to the total variability of the model output. The parameter estimation methodology we consider entails three main steps: (i) numerical solution of the ADE for a number of parameter combinations identified through a sparse grid of collocation points; (ii) derivation of a reduced complexity model of the solute breakthrough curve through the above mentioned gPCE; (iii) model calibration through Maximum Likelihood parameter estimation. Preliminary results which explore the impact of mesh adaptation on uncertainty quantification and parameter estimation are reported in [3, 40]. To the best of our knowledge this is the first time that space-time mesh adaptation is employed in the context of interpretation of solute transport phenomena in porous media.

The work is organized as follows. Section 2 introduces the problem setting, while Section 3 summarizes the key elements of the adaptive numerical methodology proposed in [44, 14]. Section 4 provides a description of the numerical implementation of the space-time mesh adaptation technique for model parameter estimation and uncertainty quantification. Results related to modeling and interpretation of solute transport within an heterogeneous sand box are provided in Section 5. Concluding remarks end the paper.

2 Problem setting

We cast the transport problem in a two-dimensional (planar) framework. The ADE reads

$$\frac{\partial C}{\partial t} + \nabla \cdot (\mathbf{v}C) - \nabla \cdot (\mathbf{D}\nabla C) = 0 \quad \text{in } \Omega \times (0,T], \tag{1}$$

where Ω is a bounded polygonal domain of $\mathbb{R}^2$, $C = C(\mathbf{x},t)$ [mol/m^3] is the unknown solute concentration at location $\mathbf{x}$ and at time t, $\mathbf{v} = (v_1, v_2)^T$ [m/s] is fluid velocity and $\mathbf{D} = \{D_{ij}\}$ is the dispersion tensor [1] given by

$$D_{ij} = (\alpha_T \|\mathbf{v}\|_2 + D_m)\,\delta_{ij} + (\alpha_L - \alpha_T)\,\frac{v_i v_j}{\|\mathbf{v}\|_2} \quad \text{with} \quad i,j = 1,2\,. \tag{2}$$

Here, α_T, α_L[m] are transverse and longitudinal dispersivity, respectively, δ_{ij} is Kronecker's delta, D_m[m^2/s] is molecular diffusion and $\|\mathbf{w}\|_2$ denotes the standard Euclidean norm of a generic vector $\mathbf{w} \in \mathbb{R}^2$. Equation (1) is completed with suitable initial and boundary conditions which, in general, can be cast as

$$\begin{cases} C(\mathbf{x},0) = C_0(\mathbf{x}) & \text{for } \mathbf{x} \in \Omega, \\ C(\mathbf{x},t) = f_1(\mathbf{x},t) & \text{for } \mathbf{x} \in \Gamma_1,\ t \in (0,T], \\ -(\mathbf{D}\nabla C)\cdot\mathbf{n} = f_2(\mathbf{x},t) & \text{for } \mathbf{x} \in \Gamma_2,\ t \in (0,T], \\ (\mathbf{v}C - \mathbf{D}\nabla C)\cdot\mathbf{n} = f_3(\mathbf{x},t) & \text{for } \mathbf{x} \in \Gamma_3,\ t \in (0,T], \end{cases} \tag{3}$$

where Γ_1, Γ_2 and Γ_3, with $\cup_{i=1}^{3}\Gamma_i = \partial\Omega$, $\Gamma_i \cap \Gamma_j = \emptyset$, for $i, j = 1, 2, 3$ and $i \neq j$, represent partitions of the boundary $\partial\Omega$ of Ω associated with Dirichlet, Neumann and Robin boundary conditions, respectively; C_0 is the initial value of the solute concentration; f_i, with $i = 1, 2, 3$, are boundary values; and $\mathbf{n}$ is the unit outward normal vector to $\partial\Omega$. A typical quantity of interest for the interpretation of experiments and field scale transport settings is the solute breakthrough curve, i.e., the time evolution of solute concentration at a fixed location. In typical experimental settings, the solute breakthrough curve is measured at the outlet section Γ_{out} of the domain and can be defined as

$$C_{out}(t) = \frac{1}{|\Gamma_{out}|}\int_{\Gamma_{out}} C\left(\mathbf{x}, t\right) d\Gamma \qquad \forall t \in [0, T], \tag{4}$$

where $|\Gamma_{out}|$ denotes the length of the outflow section. Following [14], we discretize (1)-(3) by means of a stabilized finite element method, which is based on a streamline diffusion technique [8]. Spatial discretization is performed upon relying on a spatial mesh $\mathcal{T}_h = \{K\}$, i.e., a conformal discretization of Ω into triangular elements K. Discretization of the time window $[0, T]$ is performed upon introducing the time levels $\left\{t^0, \ldots, t^n\right\}$, which define the set $\{I_k\}$ of the time intervals I_k of amplitude $\Delta t^k = t^{k+1} - t^k$, for $k = 0, \ldots, n-1$. Time discretization is performed through the standard θ-method [46]. To guarantee the unconditionally absolute stability of the θ-method, we resort to an implicit scheme and set $\theta = 2/3$.

Here we assume the velocity field $\mathbf{v}$ in (1)-(3) to be stationary and to obey Darcy's law and the fluid mass conservation equation so that

$$\begin{cases} \mathbf{v} = -\dfrac{k}{\mu\phi}\left(\nabla p + \rho g \mathbf{k}\right) & \text{for } \mathbf{x} \in \Omega, \\ \nabla \cdot \mathbf{v} = 0 & \text{for } \mathbf{x} \in \Omega, \\ \mathbf{v} \cdot \mathbf{n} = \psi & \text{for } \mathbf{x} \in \partial\Omega, \end{cases} \tag{5}$$

where p [Pa] is pressure, g [m/s^2] is gravity, $\mu > 0$ [Pa·s] and $\rho > 0$ [Kg/m^3] are the fluid viscosity and density, respectively, $k > 0$ [m^2] is the porous medium permeability (which we treat here as a generally spatially variable scalar, for simplicity), $0 < \phi < 1$ is porosity, ψ is a flux imposed on the domain boundary and $\mathbf{k}$ denotes the unit vector aligned with the vertical direction. Following [14], the numerical solution of the flow problem (5) is obtained through a mixed two-field formulation (see, e.g., [32]), based on zero-order Raviart-Thomas finite elements [7] to discretize the velocity and standard finite elements of degree zero for the pressure.

3 The adaptive discretization technique

We solve numerically the ADE (1) upon relying on an adaptive and automatic selection of the space-time discretization. The adaptive methodology we implement has been developed for shallow-water modeling in [43, 44]. A preliminary

application to transport in porous media is provided in [14]. We recount here the main concepts underlying the adaptive methodology and refer to [14] for additional details. The adaptive technique is grounded on the definition of an *a posteriori* error estimator for the global (space-time) discretization error

$$\eta_{ht}^{A} = \eta_{h}^{A} + \eta_{t}, \tag{6}$$

which includes an estimator (η_h^A) for the the approximation error associated with the spatial discretization and one (η_t) for the error due to time discretization. We assume here that the two error estimates can be computed separately, following, e.g., [34, 48]. We employ an anisotropic spatial error estimate η_h^A, i.e., an error estimate which allows optimizing not only the size but also the shape and the orientation of the mesh elements.

To compute (6), we rely on recovery-based error estimates, following the idea proposed by [58] in the context of linear elasticity. Recovery-based error estimation entails two steps: (i) local reconstruction of the solution gradient upon averaging or re-interpolating the discrete solution gradient (gradient recovery procedure), and (ii) estimation of the discretization error in the $H^1(\Omega)$-seminorm, obtained by computing the $L^2(\Omega)$-norm of the difference between the recovered gradient and the discrete gradient [59, 60]. A standard notation is here adopted for the Sobolev spaces, as well as for the space of the functions bounded almost everywhere in Ω [30]. Recovery-based estimators are typically robust and reliable and have been successfully applied to a wide spectrum of differential problems, e.g., in [17, 37, 43, 38, 54] and references therein.

3.1 Anisotropic mesh adaptation

We provide here a suitable definition of the spatial error estimator η_h^A in (6). Let C_h be the finite element approximation of concentration C, obtained by the discretization of (1). Following the approach proposed in [44, 36], we introduce the local anisotropic error estimator

$$\begin{aligned}\left[\eta_K^A(t)\right]^2 = \frac{1}{\lambda_{1,K}\lambda_{2,K}} \int_{\Delta_K} \{ \lambda_{1,K}^2 \left[\mathbf{r}_{1,K} \cdot (P_R(C_h(t)) - \nabla C_h(t))\right]^2 + \\ \lambda_{2,K}^2 \left[\mathbf{r}_{2,K} \cdot (P_R(C_h(t)) - \nabla C_h(t))\right]^2 \} \, d\Delta_K \quad \forall K \in \mathcal{T}_h, \forall t > 0, \end{aligned} \tag{7}$$

where $\lambda_{i,K}$ and $\mathbf{r}_{i,K}$, $(i = 1, 2)$, identify the eigenvalues and the eigenvectors of the tensor $\mathbf{M}_K$, defining the mapping between a reference triangle $\widehat{K}$ and the generic element K of the mesh $\mathcal{T}_h$ (see Figure 1a). Note that $\lambda_{i,K}$ measure the length of the semi-axes of the ellipse circumscribing K, while $\mathbf{r}_{i,K}$ identify the directions of these semi-axes [18, 19]. The quantity $P_R(C_h(t))$ represents the recovered spatial gradient of C_h at time t. As depicted in Figure 1b, $P_R(C_h)$ is computed as the area-weighted average of the discrete gradient ∇C_h within the patch Δ_K of triangles sharing at least one vertex with K. Thus, the global error

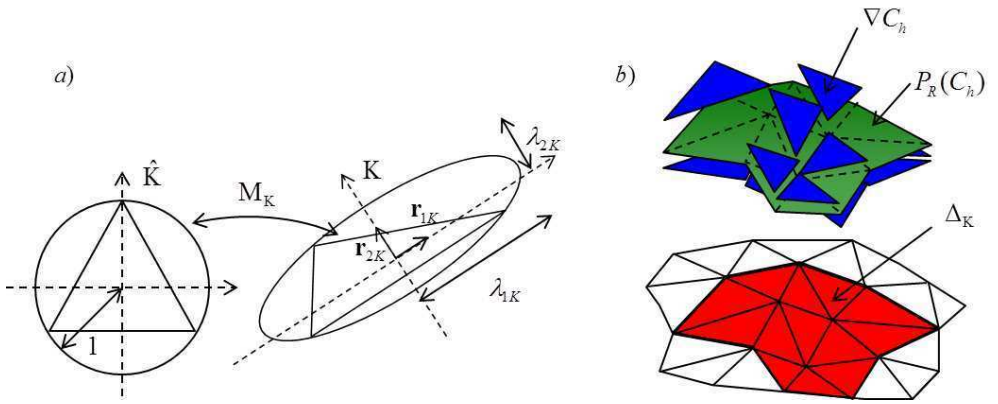

Figure 1: Spatial error estimator η_K^A (7): geometric definition of the anisotropic setting, a), definition of the recovered gradient $P_R(C_h)$, b).

estimator associated with the spatial discretization is computed as

$$\left[\eta_h^A(t)\right]^2 = \sum_{K\in\mathcal{T}_h} \left[\eta_K^A(t)\right]^2 \quad \forall t > 0. \tag{8}$$

Equation (8) represents an anisotropic error estimate, as it directly involves the anisotropic quantities $\lambda_{i,K}$ and $\mathbf{r}_{i,K}$ identifying the size, shape and orientation of element K. Note that definition (7)-(8) stems from the generalization of the standard estimate for the $H^1(\Omega)$-seminorm of the discretization error to an anisotropic setting [36, 14]. For a rigorous presentation of the error estimator (7)-(8) we refer to [43, 36].

The goal of our mesh adaptation technique is to build an anisotropic spatial grid that is driven by the estimator (7)-(8). This is achieved through the implementation of the mesh adaptation procedure presented in [19], and successively applied in several works, e.g., [34, 36, 43, 44]. The main goal of this procedure is to find the mesh with the least number of elements and associated with a fixed accuracy τ_h, i.e., such that $\eta_h^A \simeq \tau_h$ while guaranteeing an equidistribution of the error in space. A metric-based adaptation technique is applied to this end. Let $\widetilde{\mathbf{M}} : \Omega \to \mathbb{R}^{2\times 2}$ be a symmetric positive definite tensor field and $\mathcal{T}_h^b$ be a generic grid, here defined as background grid. The tensor $\widetilde{\mathbf{M}}$ can be cast as $\widetilde{\mathbf{M}} = \widetilde{\mathbf{R}}^T\widetilde{\mathbf{\Lambda}}^{-2}\widetilde{\mathbf{R}}$, where $\widetilde{\mathbf{\Lambda}} = \text{diag}\left(\widetilde{\lambda_1}, \widetilde{\lambda_2}\right)$ and $\widetilde{\mathbf{R}}^T = [\widetilde{\mathbf{r}_1}, \widetilde{\mathbf{r}_2}]$ are a positive diagonal and an orthonormal tensor, respectively defined at each $\mathbf{x} \in \Omega$. The quantities $\widetilde{\mathbf{\Lambda}}$ and $\widetilde{\mathbf{R}}$ can be approximated through matrices which are piecewise constant on $\mathcal{T}_h^b$, such that $\widetilde{\lambda}_i\big|_K = \widetilde{\lambda}_{i,K}, \widetilde{\mathbf{r}}_i\big|_K = \widetilde{\mathbf{r}}_{i,K}$, for $i = 1, 2$ and for any element K of the mesh $\mathcal{T}_h^b$. The computation of the elemental metric $\widetilde{\mathbf{M}}_K^{new}$ identifying the new adapted mesh is then performed on the background grid $\mathcal{T}_h^b$ by (i) applying an error equidistribution criterion, and (ii) solving a local constrained optimization problem on each element K of $\mathcal{T}_h^b$. In details, first the

ADE is solved on the background mesh $\mathcal{T}_h^b$. Then, the unknown metric $\widetilde{\mathbf{M}}^{new}$ is computed by imposing the desired accuracy τ_h and by equidistributing the error so that the local accuracy $\tau_K = \tau_h / N_{el}^b$ is guaranteed, N_{el}^b being the number of elements of $\mathcal{T}_h^b$. This procedure essentially leads to deal with local constrained optimization problems which can be explicitly solved [19].

Once $\widetilde{\mathbf{M}}^{new}$ is computed, the new mesh $\mathcal{T}_h^{new}$ is generated through the software BAMG [24]. We refer to [36, 43] for a detailed description of the local optimization problem and the explicit computation of the metric field from the estimator η_h^A.

Three constraints are imposed to the mesh adaptation procedure, to guarantee the robustness of the methodology. Excessive element clustering is locally prevented by setting a minimum threshold q_{min} for the product $\widetilde{\lambda}_{1,K}\widetilde{\lambda}_{2,K}$ within the local optimization solution. This is equivalent to assign a lower limit on the element area, since $|K| = |\widehat{K}|\lambda_{1,K}\lambda_{2,K}$. Two global constraints are then imposed on the minimum and maximum number of mesh elements. We set $N_{el,min} \leq N_{el}^{new} \leq N_{el,max}$, to prevent global excessive coarsening/refinement of the spatial mesh. This objective is achieved through a uniform scaling of the computed metric field $\widetilde{\mathbf{M}}^{new}$. Notice that, to contain the computational cost of the global adaptive procedure, we do not employ any iterative algorithm to obtain the new adapted mesh $\mathcal{T}_h^{new}$. As explained in Section 3.3, the adaptive procedure here detailed is applied at each time t^k to generate a corresponding adapted mesh $\mathcal{T}_h^k$.

3.2 Time step adaptation

Time step adaptation is implemented upon relying on a recovery-based estimate of the time discretization error. We aim at predicting the time step Δt^k that can be used at each time level t^k for the subsequent time advancement. For this reason we will deal only with a local time error estimator. The time step adaptation procedure entails three steps: (i) computation of a recovered time derivative, (ii) evaluation of the local time estimator, and (iii) prediction of the next time step size.

The recovery-based estimator for the time discretization error within time interval $I_{k-1} = \left[t^{k-1}, t^k\right]$ is then defined as [44, 14]

$$\left[\eta_{I_{k-1}}^T(\mathbf{x})\right]^2 = \Delta t^{k-1} \int_{I_{k-1}} \left| \frac{\partial C_R(\mathbf{x})}{\partial t}\Big|_{I_{k-1}} - \frac{C_h^k(\mathbf{x}) - C_h^{k-1}(\mathbf{x})}{\Delta t^{k-1}} \right|^2 dt, \qquad (9)$$

where $C_R(\mathbf{x})$ is a recovered solution, coinciding with the parabola which interpolates the concentration values $\left[C_h^{k-2}(\mathbf{x}), C_h^{k-1}(\mathbf{x}), C_h^k(\mathbf{x})\right]$ at t^{k-2}, t^{k-1}, t^k, respectively; and $C_h^k(\mathbf{x})$ is the numerically computed concentration at time t^k and at point $\mathbf{x}$. Note that the multiplicative factor Δt^{k-1} in (9) renders the time error estimator dimensionless, consistent with the spatial error estimator η_h^A (8).

In our finite element framework, estimator (9) is computed at specific spatial locations identified by the vertices V_i of the current grid $\mathcal{T}_h^k$. This provides us with a spatially distributed quantity, which is then lumped into a single error indicator through an area-weighted average

$$\left[\eta^T_{I_{k-1}}\right]^2 = \frac{\sum\limits_{K\in\mathcal{T}_h^k}\left[\eta^T_{I_{k-1},K}\right]^2|K|}{\sum\limits_{K\in\mathcal{T}_h^k}|K|} \tag{10}$$

where $\left[\eta^T_{I_{k-1},K}\right]^2$ is the average of estimator (9) on K computed as

$$\left[\eta^T_{I_{k-1},K}\right]^2 = \frac{1}{3}\sum_{V_i\in K}\left[\eta^T_{I_{k-1}}(V_i)\right]^2. \tag{11}$$

To compute the new time step, we assign a fixed tolerance for the time error, i.e., we impose the condition $\eta^T_{I_{k-1}} = \tau_t^{\Delta t}$. Note that the error control is applied on the time slab I_{k-1}, because the global error estimator can be evaluated only at the end of the simulation when the whole time partition is known. Following [44, 14], the adaptive time step is then calculated as

$$\Delta t^k = \frac{\tau_t^{\Delta t}}{\eta^T_{I_{k-1}}}\Delta t^{k-1}. \tag{12}$$

A minimum (Δt_{min}) and a maximum (Δt_{max}) value for the predicted time step are fixed a priori, i.e., the time step computed through (12) is constrained within an interval $[\Delta t_{min}, \Delta t_{max}]$. These lower and upper bounds for the time step are defined according to the characteristic time scale of the considered transport setting.

3.3 Solution-adaptation coupling

We outline here the numerical technique employed to couple the mesh and time step adaptation methodologies described in Sections 3.1-3.2 with the numerical approximation of the ADE (1). The procedure is graphically depicted in Figure 2 (right side).

Approximating the ADE requires (i) setting appropriate boundary and initial conditions, and (ii) knowledge of the velocity field. The latter is obtained by solving the flow problem (5) on a sufficiently fine uniform mesh $\mathcal{T}_h^0$. At a generic time t^{k-1}, the approximate concentration field C^{k-1}, the mesh $\mathcal{T}_h^{k-1}$ and the time step Δt^{k-1} are known. As a first step the ADE is numerically solved on $\mathcal{T}_h^{k-1}$. This yields the approximation $\widetilde{C}^k$ at time t^k. This approximation is used to adapt the spatial grid through the methodology described in Section 3.1. Once the metric $\widetilde{\mathbf{M}}^k = \widetilde{\mathbf{M}}^{new}$ is computed, the new mesh $\mathcal{T}_h^k = \mathcal{T}_h^{new}$ is

generated by BAMG [24]. The concentration field is then projected from $\mathcal{T}_h^{k-1}$ to $\mathcal{T}_h^k$ through an L^2-conservative projection method [43, 14]. This yields the actual approximation C^k of the concentration C at time t^k . The time step Δt^k is then predicted through the methodology described in Section 3.2. Note that, since three successive solutions are required to compute Δt^k, we fix $\Delta t^k = \Delta t_{min}$ for $k = 1, 2$.

4 Parameter estimation and uncertainty quantification

We briefly describe here the procedure we employ for model parameter estimation, which is coupled to the adaptive discretization technique described in Section 3. The method we implement combines the model reduction technique explored in [20] with a standard Maximum Likelihood parameter estimation framework [10]. To simplify the discussion of the methods, we assume here the target output quantity of interest to be the solute breakthrough curve. The extension of the methodology to other model output quantities (e.g., concentration profiles, spatial concentration fields) is straightforward.

4.1 Maximum likelihood parameter estimation

We assume a set of measurements to be available, describing the evolution in time of solute concentration at specific locations within a porous system. For our purposes, we assume that N observations of solute concentration $C^*_{out}(t_i)$ with $i = 1 \dots N$ are available at the outlet of an experimental cell. The numerical approximation of (1) yields a set of values $C_{out}(t_i, \mathbf{p})$, where $\mathbf{p}$ is a vector collecting M unknown model parameters to be estimated. We focus here on the assessment of the Maximum Likelihood (ML) estimate $\widehat{\mathbf{p}}$ of $\mathbf{p}$, which yields the ML breakthrough curve associated with the discrete values $\widehat{C}_{out}(t_i)$.

We consider measurement errors to be Gaussian, and that no cross correlation exists between errors associated with measurements $C^*_{out}(t_i)$ acquired at different times. We further assume that the covariance matrix of estimation errors

$$\mathbf{C}_C = \sigma_C^2 \mathbf{V} \tag{13}$$

is known up to a positive constant σ_C^2 and that the prior estimation error of concentration is constant in time, i.e., $\mathbf{V} = \mathbf{I}$, $\mathbf{I}$ being the identity matrix.

Given the above assumptions, the ML estimate $\widehat{\mathbf{p}}$ is obtained upon minimizing the Negative Log Likelihood

$$NLL = \frac{J}{\sigma_C^2} + N \log \sigma_C^2 + N \log (2\pi) \tag{14}$$

with

$$J(\mathbf{p}) = \sum_{i=1}^{N} \left[C_{out}(t_i, \mathbf{p}) - C^*_{out}(t_i) \right]^2 . \tag{15}$$

We can then compute

$$\widehat{\sigma}_C^2 = \frac{J\left(\widehat{\mathbf{p}}\right)}{N} \tag{16}$$

which corresponds to the a posteriori ML estimate of the measurement error variance.

The covariance matrix associated with parameter estimates is then computed as [10]

$$\mathbf{Q} = \widehat{\sigma}_C^2 \left(\mathbf{J}\mathbf{V}\mathbf{J}^T\right)^{-1} \tag{17}$$

where $\mathbf{J}$ is a Jacobian matrix, which contains the derivatives with respect to the input parameters of the output concentrations forming the breakthrough curve at the N observation times t_i.

4.2 Modeling procedure

A large number of model evaluations is typically required to minimize (14) and to compute numerically the Jacobian $\mathbf{J}$ in (17). For this reason, we approximate the numerical breakthrough curve $C_{out}(t_i, \mathbf{p})$ in (14)-(15) with a reduced complexity surrogate model, $C_{out}^{PC}(t_i, \mathbf{p})$. The surrogate model for $C_{out}(t_i, \mathbf{p})$ is expressed in terms of a generalized polynomial chaos expansion (gPCE) ([53] and references therein), which can be cast as

$$C_{out}^{PC}(t_i, \mathbf{p}) = \sum_{j=1}^{Q} \beta_j \psi_j(\mathbf{p}) \tag{18}$$

where β_j are the so-called gPCE coefficients, ψ_j is a set of multivariate orthogonal polynomials and Q is the total number of polynomials included in the expansion. The polynomial basis ψ_j is selected as a function of the probability density function model assigned to the uncertain input parameters [53]. In this work we assume that the uncertain parameters collected in $\mathbf{p}$ are characterized by uniform distributions. Hence, we select ψ_j as Legendre orthogonal polynomials.

We provide in the following a complete overview of the modeling procedure we employ, which combines the numerical methodologies introduced in Sections 3 with the model reduction, parameter estimation and uncertainty quantification steps. The overall procedure entails the five steps described in the following (see Figure 2).

a) **Identification of calibration parameters and related domain of variability.** As a first step, a set of M unknown parameters needs to be identified. These may include the local dispersivities, porosities and permeabilities of the porous medium. A lower and an upper bound of variability are introduced for each parameter to define a multidimensional parameter space Γ_P.

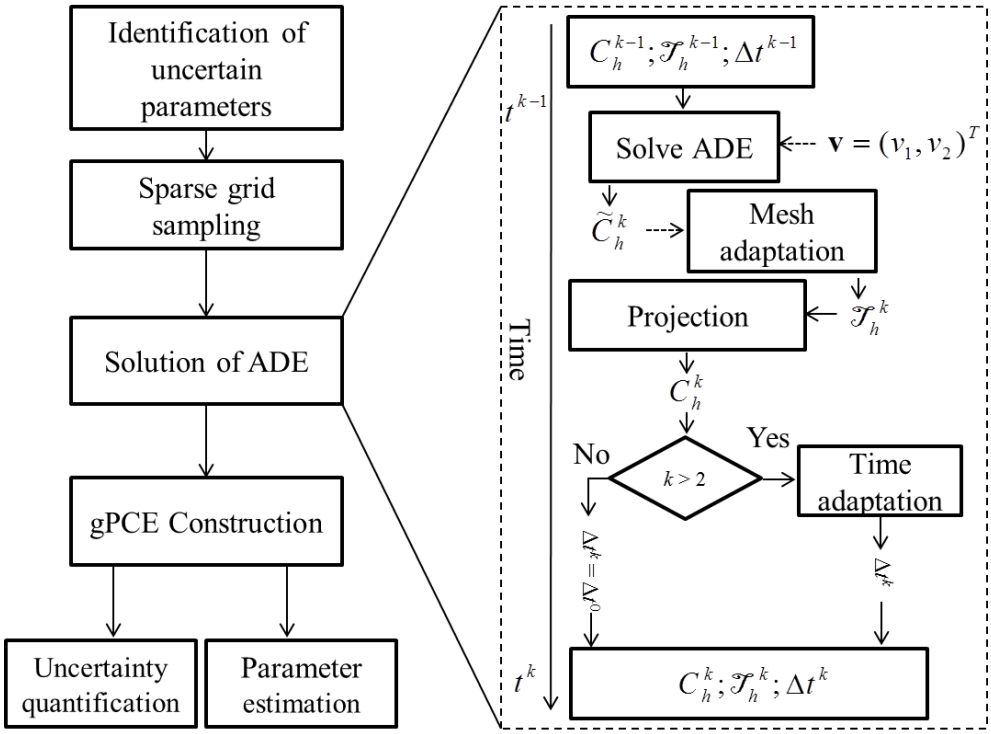

Figure 2: Sketch of the numerical procedure.

b) **Sparse grid sampling.** A number N_C of collocation points is selected within the M-dimensional parameter space Γ_P by means of a sparse grid sampling technique, along the lines of [20]. Each collocation point corresponds to a coordinate in Γ_P, i.e., it is associated with specific values of the selected uncertain model parameters.

c) **Forward simulation.** A forward simulation of the ADE (1) is performed for parameter values corresponding to each collocation point. This simulation step can be performed through the space-time adaptive methodology described in Section 3 (see Figure 2, right) or by means of standard (fixed and uniform) meshes.

d) **Model reduction.** The gPCE (18) of the model output is obtained following the methodology outlined in [20], where the coefficients β_j are computed through algebraic manipulations of the model evaluations obtained at each of the N_C collocation points. This provides us with a reduced complexity (surrogate) model of the solute breakthrough curve.

e) **Parameters estimation.** The gPCE expansion is then used as a proxy of the original system model for the minimization of the NLL criterion (14). The minimization of (14) is here performed by means of the Nelder-

Mead simplex search method [28], implemented in the Matlab function `fminsearch`. This allows computing the ML parameter estimate $\widehat{\mathbf{p}}$. The related uncertainty is evaluated through an analytical computation of the covariance matrix $\mathbf{Q}$ (17).

f) **Global sensitivity analysis and uncertainty quantification.** We exploit the gPCE model to obtain a large set of Monte Carlo realizations of the breakthrough curve at a reduced computational cost. This allows propagating to the output quantity of interest the uncertainty associated with ML parameter estimates. It additionally enables us to analytically compute from the gPCE the variance-based Sobol sensitivity indices [49, 50]. These indices yield a quantitative measure of the way the variability of the model output is influenced by the variability of each of the considered uncertain parameters. The definition of the Sobol indices and their relationship with the gPCE representation (18) is recalled in Appendix A for completeness.

The accuracy of approximation (18) increases with the number Q of terms included in the expansion [20]. This is in turn linked to the largest polynomial order w selected for the gPCE surrogate model. Recent works [15, 11] show that expression (18) with the assumptions we employ for the probability distributions of the uncertain model parameters constitutes a viable representation of the output of solute concentrations at laboratory scales.

5 Numerical results

This section is devoted to the assessment of the effect of the space-time adaptation methodology introduced in Section 3 on the estimation of the longitudinal dispersivity coefficients for the interpretation of a laboratory-scale solute transport experiment performed in a block-wise heterogeneous sandy porous medium. In the following we first provide a brief description of the experimental data-set. We then present the application of the space-time adaptive methodology to the forward simulation of the transport process. Finally, we assess the impact of the space-time adaptive methodology on the results of the parameter estimation procedure. We do so upon comparing the results of parameter estimation obtained by means of a mesh with fixed uniform discretization (i.e., fixed uniform spatial mesh and time step) and our space-time adaptive methodology.

5.1 Overview of the Experiment and Data set

We consider transport of a nonreactive solute within a flow cell packed with two different sand types. Figure 3 depicts a sketch of the experimental set-up. The dataset we examine is part of a still unpublished set of experiments which was provided to us courtesy of Professor Brian Berkowitz, Weizmann Institute of

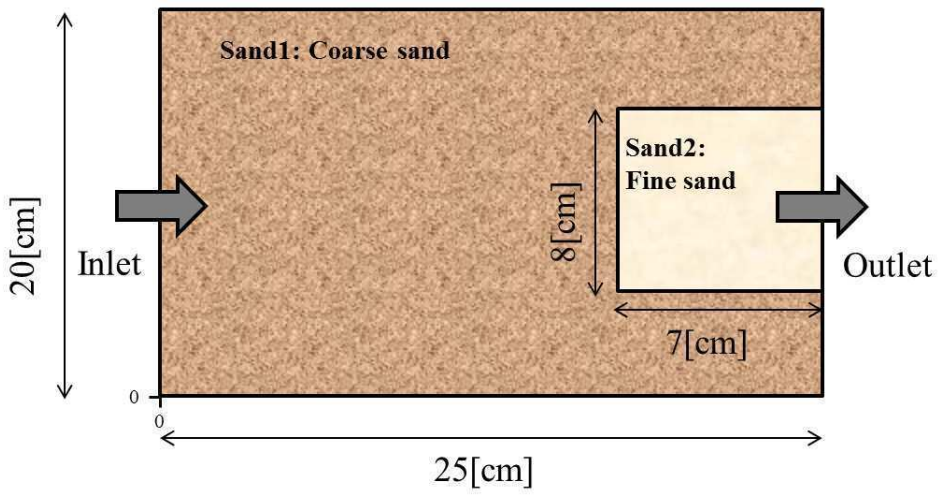

Figure 3: Experimental flow cell: definition sketch.

Science. The experiment we consider is conducted in a rectangular flow cell of size $0.25 \times 0.20\text{m}^2$, characterized by a constant thickness of 0.01 m. Inflow and outflow to the cell are formed by a cylindrical tube with circular cross-section of diameter equal to 4 mm and are located in the middle of the left and right sides of flow cell (see Figure 3). The experimental data are solute breakthrough concentrations which are acquired at the outlet with the same methodology presented in [29].

The packing comprises a rectangular-shaped region near the outlet, filled with a fine well-rounded quartz sand (sand 2) with grain diameter of 0.231 mm and hydraulic conductivity of 0.014 cm/s, within a background coarser sand (sand 1) with grain diameter of 1.105 mm and hydraulic conductivity of 0.5 cm/s [29].

Steady state flow is established in the cell at a constant flow rate of $Q_{in} = 4.6$ ml/min. The flow cell is initially saturated with water. A solution containing a constant tracer concentration C_0 is introduced as a step-input at the inlet at time $t = 0$. The tracer breakthrough curve is measured by means of an electrical conductivity meter at the outlet. We consider here the data stemming from three replicates of the transport experiment.

5.2 The adaptive mesh procedure

We illustrate here the results obtained by applying the adaptive methodology described in Section 3 to the forward simulation of the experimental setting described in Section 5.1. The velocity field is obtained upon numerically solving the flow equations (5), as discussed in Section 2. A high resolution velocity field is computed on a fine uniform grid of about 95000 elements. A constant

(atmospheric) pressure is imposed at the outlet boundary. We set $\mathbf{v}\cdot\mathbf{n} = Q_{in}/A_{in}$ at the inlet, A_{in} being the area of the inflow cross section. The remaining parts of the boundary of the flow cell are impermeable. For the sake of our demonstration, we set the porosities of the coarse and fine sands to $\phi_1 = 0.41$ and $\phi_2 = 0.38$, respectively, upon preliminary visual calibration of the breakthrough curve. We set the fluid viscosity μ and density ρ to 10^{-3} Pa·s and 1000 kg/m^3, respectively.

Figure 4 depicts the concentration field obtained by simulating the transport experiment through the adaptive methodology together with the corresponding adapted meshes. In particular, we consider the time window $t \in [0, 6000]$ s. Figures 4a-c illustrate the temporal evolution of the concentration field. At early times, the solute spreads radially into the cell around the inflow section (see Figure 4a). Then, the concentration front deforms and displaces towards the middle of the cell (see Figure 4b) under the effect of advective and dispersive processes. At time $t \approx 1200$ s the solute starts reaching the low conductivity inclusion, located near the outlet section. The difference between hydraulic conductivities of the coarse and fine sand regions induces a locally complex pattern of the solute concentration field (see Figure 4c). Two main mechanisms contribute to solute mass transfer between the two regions (see Figure 4g): (i) the advective flow field tends to drive the concentration front around the low permeability block, while (ii) diffusive/dispersive mass transfer takes place along the left-hand side of the inclusion, located at $x = 0.18$ m and parallel to the y-axis. As a consequence of the interplay between these two mechanisms, we observe the appearance of an arrow-shaped region associated with small concentration values in the fine sand block, while two sharp concentration fronts develop parallel to the x-axis, along the upper and lower edges of the interface (located at $y = 0.06$ m and $y = 0.14$ m). The local concentration gradients observed in Figure 4g tend to gradually smooth out for longer times. The last regions of the cell which are reached by the invading solute are located at the bottom- and top-right corners of the domain (not shown).

Figure 4d)-f) shows the adapted computational mesh corresponding to the solutions at the time-frames depicted in Figure 4a-c. The adaptive simulation is obtained upon setting the tolerances $\tau^S = 1.5$ (for spatial mesh adaptation) and $\tau^T_{\Delta t} = 0.17$ (for time step adaptation), $N_{el,min} = 1000$ and $N_{el,max} = 10000$, the lower and upper bounds for the time step being fixed to $\Delta t_{min} = 1$ s and $\Delta t_{max} = 30$ s, respectively. As discussed in [14], the value q_{min} set as a local constraint plays a key role for an accurate approximation of the breakthrough curve. We recall that parameter q_{min} corresponds to the minimum allowed value of the product $\lambda_{1,K}\lambda_{2,K}$. We observe that (i) an accurate discretization of the concentration field at the inlet is critical to capture solute behavior at early times; (ii) high mesh resolution is required to capture the propagation of the solute at the interface between the two regions with contrasting conductivities; and (iii) a proper discretization of the concentration at the outlet section is key for a sound comparison between the numerical results and the experimental

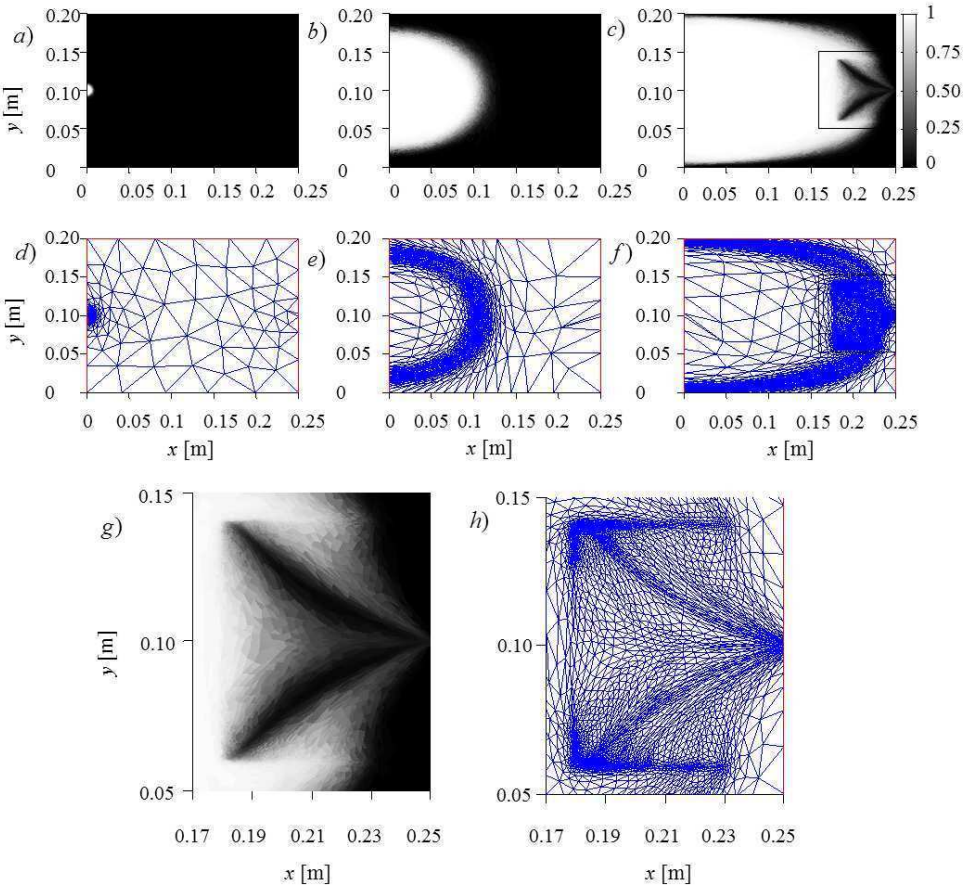

Figure 4: Adaptive forward simulation: snapshots of concentration field a)-c), and corresponding adapted meshes d)-f). Results are for $t = 4$s a),d), $t = 760$s b),e) and $t = 1900$s c),f). A zoom on the regions highlighted in c),f) is shown in g),h).

measurements (i.e., the measured breakthrough curve). As a consequence, we adaptively modify the value of q_{min} along the simulated time window according to the following strategy: (i) for $t < 50$ s we set $q_{min} = 10^{-9}$ m^2 to properly model the concentration field near the inflow section; (ii) we increase q_{min} to 10^{-6} m^2 for intermediate times to minimize computational resources, and (iii) we set $q_{min} = 10^{-9}$ m^2 as soon as the ratio C/C_0 exceeds the threshold $\epsilon = 10^{-3}$ at any position in the low conductivity block. This latter value for q_{min} is then preserved until the end of the simulation.

We observe that the generated computational meshes follow the temporal evolution of the concentration front (see Figure 4d-f) and allow capturing the local patterns of the spatial distribution of concentration in the cell (see Figure 4h). Anisotropic adaptation allows optimizing the mesh with respect to

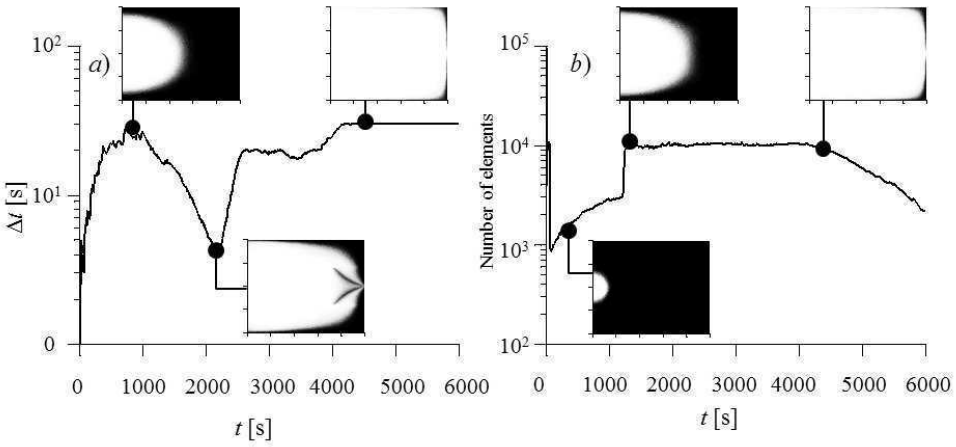

Figure 5: Adaptive forward simulation: temporal evolution of the time step Δt a), and of the cardinality of the adapted spatial mesh b). Inserts show snapshots of the concentration field.

the directional features of the solution, as documented by the highly stretched triangles generated along the concentration front (see, e.g., Figure 4h).

Figure 5 depicts the evolutions of the time step and of the spatial mesh cardinality along the simulation time, and relates these with the dynamics of the transport phenomenon. The following three stages are observed:

- For $t < 1200$ s we observe a smooth spreading of the front within the homogeneous coarse sand domain. Hence, the time step increases from the minimum value $\Delta t_{min} = 1$ s to $\Delta t = 25$ s (Figure 5a) and the number of mesh elements is comprised between 1000 and 3000 (Figure 5b).

- For 1200s$< t < 3500$ s the transport phenomenon exhibits complex dynamics, as illustrated in the snapshots depicted in Figure 5a and in Figure 4g. As a consequence, the time step size reduces and attains a minimum value $\Delta t = 5$ s at $t \approx 2000$ s before increasing gradually (Figure 5a), while the number of mesh elements sharply increases to the maximum allowed number, i.e. $N_{el,max} = 10000$ (Figure 5b). Note that this sudden increase of the mesh cardinality is associated with the change in the parameter q_{min} from 10^{-6} m^2 to 10^{-9} m^2, which allows capturing fine details of the numerical solution at the interface between the two regions (see Figure 4g-h).

- For long times ($t \geq 3500$s), the concentration front is localized in a very small portion of the domain. Hence, we observe again an increase of the time step, which attains a maximum value $\Delta t_{min} = 30$ s at $t \approx 4000$ s (Figure 5a) and then preserves this value until the end of the simulation. At the same time, a progressive decrease of the number of elements is

observed. The number of mesh elements is equal to 2000 at the end of the simulation (Figure 5b).

5.3 Parameter estimation

We apply here the methodology introduced in Section 4.2 to estimate the longitudinal dispersivities α_{L1} and α_{L2} associated with the coarse and the fine sand, respectively. We assume that quantities $\log_{10}(\alpha_{Li})$ $(i = 1, 2)$ are uniformly distributed within the interval $[-6, -2]$, with α_{Li} given in meters. For our illustration purposes, we set transverse dispersivities to the commonly employed values $\alpha_{Ti} = \alpha_{Li}/10$. The gPCE approximation of the solute breakthrough curve is obtained by means of a polynomial of order $w = 3$ so that the parameter space is sampled through 29 collocation points, i.e., the ADE is solved for 29 different pairs of longitudinal dispersivity values (details not shown). To assess the impact of the space-time adaptive methodology, the simulation step is performed through two different discretization strategies: (i) a fixed uniform space-time discretization, and (ii) the adaptive discretization introduced in Section 3. The numerical constraints imposed to the space-time adaptive procedure are fixed for all simulations and coincide with those illustrated in Section 5.2. The fixed uniform space-time mesh comprises 50000 triangles and a constant time step $\Delta t = 1$ s is employed. Note that the number of elements of the fixed uniform spatial mesh is five times larger than the maximum number of elements ($N_{el,max}$) allowed for the adaptive anisotropic mesh, while the uniform time step Δt coincides with the lower bound Δt_{min} for the time step adaptive procedure. The resolution of the fixed uniform spatial grid and time step are chosen upon a preliminary analysis on the accuracy of the numerical solution.

Table 1 lists the results of ML parameter estimation and global sensitivity analysis. It includes the optimized value of the NLL criterion, the estimated measurement error variance $\widehat{\sigma}^2_C$, the ML estimates $\log_{10}(\widehat{\alpha}_{Li})$, and the associated estimation variances $\widehat{\sigma}^2[\log_{10}(\alpha_{Li})]$, corresponding to the diagonal terms of the covariance matrix $\mathbf{Q}$ in (17), as well as the time-averaged total Sobol indices associated with the two longitudinal dispersivities. All results are listed for both a space-time fixed uniform and adaptive discretizations. The ML estimates $\widehat{\alpha}_{Li}$ obtained via the two approaches are within the same order of magnitude. However, we observe that the use of space-time adaptation allows improving the quality of parameter estimation results: the optimized value of the NLL is reduced by about 10%, and the uncertainty associated with both ML parameter estimates obtained by space-time adaptation is smaller than the one associated with the fixed uniform discretization. In particular we observe that the variance associated with $\widehat{\alpha}_{L2}$ is largely reduced by implementing the adaptive technique.

Figure 6 shows the comparison between experimental data and the breakthrough curves resulting from ML parameter estimation. Both the gPCE approximation of the breakthrough curve resulting from parameter estimation (continuous lines) and the results obtained by a full model run with the estimated

Table 1: Results of parameter estimation and global sensitivity analysis: optimized value of NLL criterion, ML estimates of $\log_{10}\widehat{\alpha}_{Li}$ and corresponding estimation variance $\widehat{\sigma}^2$, and time average $\overline{S}_T$ of the total Sobol sensitivity indices associated with the two dispersivities. Results are listed for a space-time fixed uniform and adaptive discretization.

Discretization	NLL	$\widehat{\sigma}^2_C$	Parameter	$\log_{10}\widehat{\alpha}_{Li}$	$\widehat{\sigma}^2\,[\log_{10}\alpha_{Li}]$	$\overline{S}_T$
Fixed uniform	-571.6	9.58×10^{-4}	α_{L1}[m]	-4.33	0.68	0.98
			α_{L2}[m]	-3.95	2.24	0.02
Space-time adapted	-632.7	6.17×10^{-4}	α_{L1}[m]	-4.22	0.15	0.47
			α_{L2}[m]	-3.14	0.01	0.57

parameters (dashed lines) are graphically depicted. We observe that the calibrated gPCEs constructed for both space-time discretization strategies, i.e., fixed uniform and adaptive meshes, virtually coincide with the corresponding full model results (i.e., dashed and continuous lines are essentially superimposed in Figure 6). The mean squared error between the gPCE approximation and the full model run is equal to 7.8×10^{-5} and 3.2×10^{-6} for the space-time adaptive and fixed uniform discretization, respectively. This result shows that the gPCE model implemented renders a reliable approximation of the solute breakthrough curve for the purpose of this parameter estimation example.

We observe that the early part of the breakthrough curve ($1900 < t < 2500$ s) is represented with the same degree of accuracy by both the discretization strategies. The fixed uniform discretization leads to a marked underestimation the observed experimental data for $2500 < t < 4500$ s. The space-time adaptive approach leads to a significant reduction of the difference between modeling results and experimental data (see Figure 6), although a slight underestimation is still observed for $3500 < t < 4500$ s. This discrepancy between experimental observations and numerical results may be due to the influence of (i) additional uncertain parameters not investigated in this study (e.g., transverse dispersivity) or (ii) model error due to the inadequacy of the ADE to fully interpret transport phenomenona. Further studies on this issue would require the investigation of anomalous transport formulations and this is beyond the scope of this work. All calibrated curves shown in Figure 6 yield similar results for the longest times examined ($t > 4500$ s), i.e., the difference between experimental observations and modeling results tends to reduce with time.

Results listed in Table 1 show that the discretization strategy has a marked impact on the way uncertainty propagates from input parameters to simulation outputs. This effect can be additionally quantified upon considering the Sobol sensitivity indices obtained by applying the fixed uniform and adaptive discretizations. The time-averaged values of the total Sobol indices $S_T\,(\alpha_{Li})(i = 1, 2)$ associated with the two dispersivities are listed in Table 1, their temporal evolution being depicted in Figure 7. We observe that $\overline{S}_T\,(\alpha_{L1}) \approx \overline{S}_T\,(\alpha_{L2})$ when the space-time mesh is adapted, i.e., the influence of the two parameters on the model output is comparable on average (see Table 1). The influence of the lon-

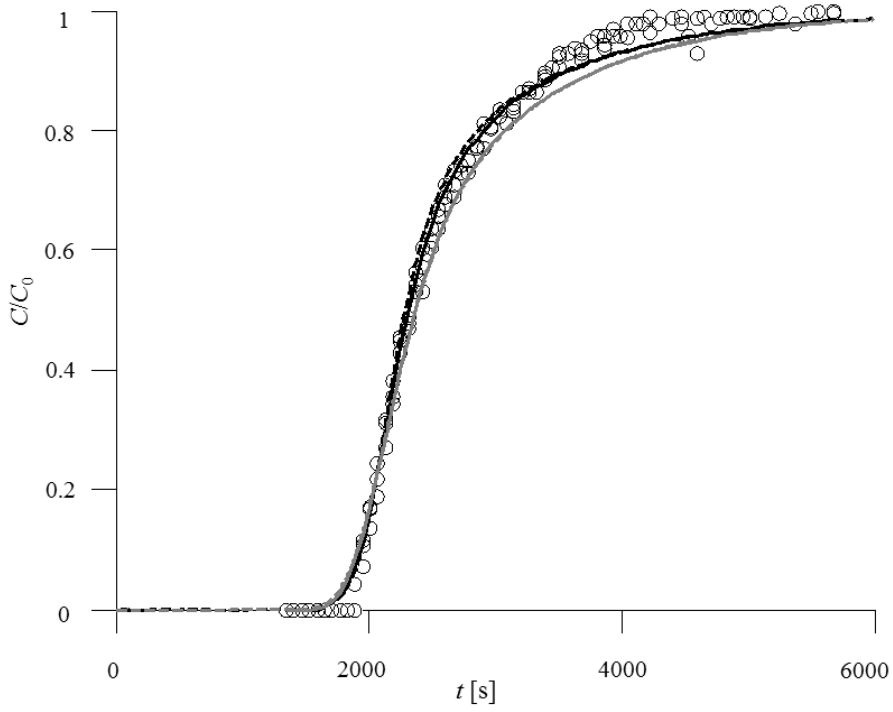

Figure 6: Parameter estimation: comparison between experimentally measured (symbols) and ML calibrated solute breakthrough curves obtained by fixed uniform (gray curves) and space-time adaptive (black curves) discretization. Continuous curves correspond to the breakthrough curve rendered by the gPCE model; dashed curves represent the result of a forward run with ML parameter estimates listed in Table 1 for each of the two discretization strategies.

gitudinal dispersivity of the low conductivity sand block (α_{L2}) tends to increase for long times (see Figure 7a)), consistent with the advancement of the solution within this region. On the other hand, the numerical breakthrough curve is basically insensitive to α_{L2} for the whole considered time window when a fixed uniform discretization strategy is implemented (see Figure 7b)). In this latter case we find $\overline{S}_T(\alpha_{L1}) \gg \overline{S}_T(\alpha_{L2})$. Note that the uncertainty bounds related to ML estimates listed in Table 1 and computed by (17) are inherently linked to the sensitivity of the output variable to the input parameters. Therefore, the observed significant difference between the two temporal evolution of the Sobol indices explains the large reduction in the uncertainty bounds associated with the estimation of $\widehat{\alpha}_{L2}$ by means of a space-time adaptive methodology.

Finally, we assess the propagation to the model output of the uncertainty related to the parameter estimation results yielded by the two discretization strategies. As a reduced complexity model, the gPCE allows for a fast evalu-

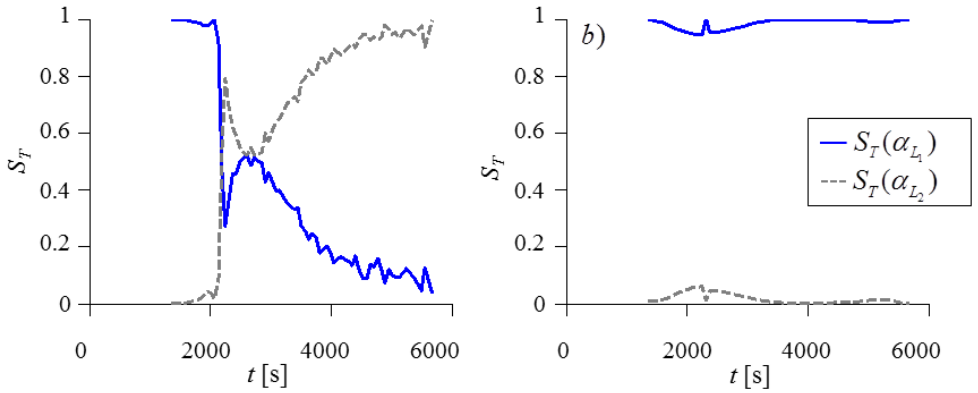

Figure 7: Global sensitivity analysis: time evolution of the total Sobol indices associated with dispersivities α_{L1}, α_{L2} obtained through space-time adaptive a) and fixed uniform b) discretizations.

ation of the solute breakthrough curve as a function of the selected uncertain parameters. Following model calibration, we consider $\log_{10}(\alpha_{Li})$ $(i = 1, 2)$ to be described by a bi-variate Gaussian distribution, centered on the ML parameters estimates $\widehat{\alpha}_{Li}$ and characterized by the covariance matrix $\mathbf{Q}$. We then perform 10^4 evaluations of the solute breakthrough curve gPCE approximation (18) in a Monte Carlo framework and compare the results yielded by the implementation of the space-time adaptive approach with those obtained by a fixed uniform discretization. Figure 8 depicts the results of this analysis. Figure 8a-b depict the Monte Carlo realizations (grey curves) together with their associated 5th and 95th percentiles (solid black curves) obtained through the space-time adaptation and the fixed grid approach, respectively. Figure 8c-e juxtaposes the empirical probability density functions (pdfs) of the normalized solute concentrations resulting from the two grid discretization strategies at three selected times. We observe that the uncertainty related to parameter estimates is largely reduced by implementing a space-time adaptive procedure in the forward simulation step with respect to a standard fixed uniform discretization in space and time. This is particularly evident for early times ($t \approx$2000 s). The results in Figure 8c-e indicate that the discretization strategy has a remarkable impact on these output pdfs. In general, the pdfs obtained by approximating the ADE through a fixed uniform discretization display a considerably larger spread than those obtained by means of an adaptive method. This result is particularly evident when we consider early solute arrivals (Figure 8c-d). For later times, (Figure 8e) we observe that the pdf associated with the fixed uniform strategy is associated with smaller concentration values than those linked to the space time adaptive methodology. At this late time the two pdfs tend to assume a similar shape. These results suggests that the impact of the choice of automatically adaptive discretization methods may be relevant in practical applications, e.g., when the

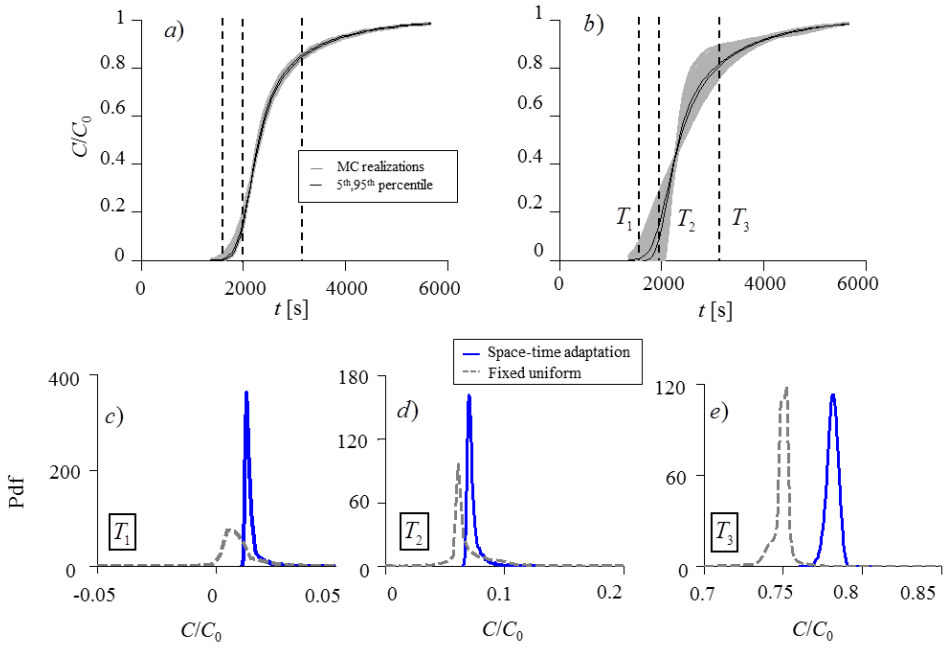

[tb]

Figure 8: Uncertainty quantification: Monte Carlo realizations of solute breakthrough curves (gray curves) obtained through the gPCE associated with the space-time adaptation method a) and the fixed uniform discretization b), and corresponding probability density functions of the normalized concentration C/C_0 at selected time levels $T_1 = 1500$s c), $T_2 = 2000$s d) and $T_3 = 3100$s e). Continuous black curves in a)-b) correspond to the time evolution of the 5th and 95th percentile of the distributions.

estimation of the risk associated with target scenarios of groundwater pollution is of concern.

6 Conclusions

We provide a methodology for forward simulation and parameter estimation of solute transport in porous media. We base our study on the standard ADE formulation. The numerical solution of the ADE is achieved by means of a space-time adaptive discretization. We implement anisotropic spatial mesh adaptation, which allows optimizing size, shape and orientation of the mesh elements with respect to the features of the numerical solution considered, together with time step adaptation. The methodology is here applied to the interpretation of a laboratory scale solute transport experiment performed within a block-wise heterogeneous sand box. Our results lead to the following major conclusions:

- The proposed adaptation procedure is robust and able to capture the evolutionary features of the target problem. We couple the space-time adaptive methodology with a model reduction technique based on a generalized Polynomial Chaos Expansion (gPCE) approximation of the considered transport model. A fixed set of constraints and tolerances allow simulating the transport process in the presence of large variations of the physical model parameters (e.g., dispersivities). This result shows that the proposed adaptive methodology is suited to be embedded in parameter estimation and/or uncertainty quantification schemes, where the input/output relationship need to be investigated through multiple numerical simulations of the transport problem.

- The impact of the space time adaptive procedure is assessed by means of maximum likelihood (ML) parameter estimation based on a set of solute breakthrough concentration measurements acquired at the outlet of the experimental flow cell. When compared to standard fixed uniform discretizations characterized by an apparently sufficient resolution, the quality of parameter estimation results improves when the space-time adaptive methodology is implemented. The space-time adaptive approach allows reducing (i) the estimated error between model predictions and experimental measurements, and (ii) the bounds of uncertainty associated with ML parameter estimates.

- Implementing a space-time adaptive methodology bears a marked impact on global sensitivity analysis and uncertainty quantification results. The sensitivity of the model output to input uncertain parameters may be highly affected by the space-time discretization strategy. In our example the total Sobol sensitivity indices associated with the longitudinal dispersivity of the low conductivity region has only a marginal influence on the solute breakthrough curve when a fixed uniform discretization strategy is implemented. On the other hand, the space-time adaptive simulation allows grasping the influence of this parameter on the output breakthrough curve. Our analysis suggests that this result may be due to the accurate space-time resolution of the adaptive discretization at the transition of the concentration front from the coarse to the fine sand region.

- As a final result, we present (empirical) probability density distributions of breakthrough concentrations, computed through Monte Carlo simulations of the constructed gPCE surrogate models. We show that implementing a space-time adaptive procedure in the considered transport setting leads to a considerable uncertainty reduction associated with the solute breakthrough at the outlet of the experimental cell. This result suggests that adaptive discretization strategies may provide a key tool for uncertainty control and reduction, to be employed, e.g., within risk assessment practice of groundwater pollution.

A Computation of Sobol indices

For the sake of the computation of the Sobol indices, we rewrite (18) upon adopting a multi-index notation. Let $\mathbf{i} \in \mathbb{N}^M$ be a multi-index vector, collecting the order of each polynomial $\psi_{\mathbf{i}}$ with respect to each parameter p_n and Λ be the set of multi-indices identifying the polynomials included in the expansion (18). We recast (18) as

$$C_{out}^{PC}(t_i, \mathbf{p}) = \beta_{\mathbf{0}}\psi_{\mathbf{0}} + \sum_{n=1}^{M}\sum_{\mathbf{i}\in\mathcal{P}_n} \beta_{\mathbf{i}}\psi_{\mathbf{i}}(\mathbf{p}) + \sum_{n=1}^{M}\sum_{m=n}^{M}\sum_{\mathbf{i}\in\mathcal{P}_{n,m}} \beta_{\mathbf{i}}\psi_{\mathbf{i}}(\mathbf{p}) \dots \tag{19}$$

where $\mathcal{P}_{n,m}$ indicates the subset of Λ for which only the m-th and n-th components of $\mathbf{i}$ are non zero, and analogously for $\mathcal{P}_n$. Equation (19) is equivalent to the ANOVA decomposition of $C_{out}(t_i)$ [50]. As a consequence the full set of Sobol indices can be analytically computed as

$$S(p_n) = \sum_{\mathbf{i}\in\mathcal{P}_n} \frac{\beta_{\mathbf{i}}^2}{V} \qquad S(p_{n,m}) = \sum_{\mathbf{i}\in\mathcal{P}_{n,m}} \frac{\beta_{\mathbf{i}}^2}{V} \tag{20}$$

where

$$V = \sum_{\mathbf{i}\in\Lambda} \beta_{\mathbf{i}}^2 - \beta_{\mathbf{0}}^2 \tag{21}$$

is total output variance. Note that the Sobol index $S(p_n)$ gathers solely the contribution of parameter p_n to the total variance V, while the index $S(p_{n,m})$ considers the combined influence of parameters p_n, p_m. The total Sobol index associated with p_n is then defined as

$$S_T(p_n) = S(p_n) + \sum_{k\neq n} S(p_n, p_k) + \sum_{k,j\neq n} S(p_n, p_k, p_j) \dots \tag{22}$$

and includes all contributions of parameter p_n to the total variance.

Acknowledgements

We kindly acknowledge Prof. Brian Berkowitz for sharing with us the experimental data. The financial support of MIUR (Project "Innovative methods for water resources under hydro-climatic uncertainty scenarios", PRIN 2010/2011) is also gratefully acknowledged.

References

[1] Bear, J., and A.-D. Cheng (2010), *Modeling Groundwater Flow and Contaminant Transport*, vol. 23, Springer.

[2] Becker, R., and R. Rannacher (2001), An optimal control approach to a posteriori error estimation in finite element methods, *Acta Numer.*, *10*, 1–102.

[3] Becker, R., M. Braack, D. Meidner, R. Rannacher, and B. Vexler (2007), Adaptive finite element methods for pde-constrained optimal control problems, in *Reactive flows, diffusion and transport*, 177–205, Springer.

[4] Berkowitz, B., A. Cortis, M. Dentz, and H. Scher (2006), Modeling non-Fickian transport in geological formations as a continuous time random walk, *Rev. Geophys.*, *44*(2).

[5] Branets, L. V., S. S. Ghai, S. L. Lyons, and X.-H. Wu (2009), Challenges and technologies in reservoir modeling, *Commun. Comput. Phys.*, *6*(1), 1–23.

[6] Bresciani, E., P. Davy, and J. Dreuzy (2012), A finite volume approach with local adaptation scheme for the simulation of free surface flow in porous media, *Int. J. Numer. Anal. Meth. Geomech.*, *36*(13).

[7] Brezzi, F., and M. Fortin (1991), *Mixed and Hybrid Finite Element Methods*, Springer New York.

[8] Brooks, A. N., and T. J. Hughes (1982), Streamline upwind/Petrov-Galerkin formulations for convection dominated flows with particular emphasis on the incompressible Navier-Stokes equations, *Comput. Methods Appl. Mech. Engrg.*, *32*(1), 199–259.

[9] Cao, J., and P. K. Kitanidis (1999), Adaptive-grid simulation of groundwater flow in heterogeneous aquifers, *Adv. Water Res.*, *22*(7), 681–696.

[10] Carrera, J., and S. P. Neuman (1986), Estimation of aquifer parameters under transient and steady state conditions: 1. Maximum likelihood method incorporating prior information, *Water Resour. Res.*, *22*(2), 199–210.

[11] Ciriello, V., A. Guadagnini, V. Di Federico, Y. Edery, and B. Berkowitz (2013), Comparative analysis of formulations for conservative transport in porous media through sensitivity-based parameter calibration, *Water Resour. Res.*, *49*(9), 5206–5220.

[12] Ciriello, V., V. Di Federico, M. Riva, F. Cadini, J. De Sanctis, E. Zio, and A. Guadagnini (2013), Polynomial chaos expansion for global sensitivity analysis applied to a model of radionuclide migration in a randomly heterogeneous aquifer, *Stoch. Environ. Res. Risk Assess.*, *27*(4), 945–954.

[13] Coupez, T., and E. Hachem (2013), Solution of high-Reynolds incompressible flow with stabilized finite element and adaptive anisotropic meshing, *Comput. Methods Appl. Mech. Engrg.*, *267*, 65–85.

[14] Esfandiar, B., G. Porta, S. Perotto, and A. Guadagnini (2014), Anisotropic mesh and time step adaptivity for solute transport modeling in porous media, in *New Challenges in Grid Generation and Adaptivity for Scientific Computing*, Springer, in press.

[15] Fajraoui, N., F. Ramasomanana, A. Younes, T. A. Mara, P. Ackerer, and A. Guadagnini (2011), Use of global sensitivity analysis and polynomial chaos expansion for interpretation of nonreactive transport experiments in laboratory-scale porous media, *Water Resour. Res.*, *47*(2).

[16] Fajraoui, N., T. A. Mara, A. Younes, and R. Bouhlila (2012), Reactive transport parameter estimation and global sensitivity analysis using sparse polynomial chaos expansion, *Water Air Soil Pollu.*, *223*(7), 4183–4197.

[17] Farrell, P., S. Micheletti, and S. Perotto (2011), An anisotropic Zienkiewicz–Zhu-type error estimator for 3d applications, *Int. J. Numer. Meth. Engng.*, *85*(6), 671–692.

[18] Formaggia, L., and S. Perotto (2001), New anisotropic a priori error estimates, *Numer. Math.*, *89*(4), 641–667.

[19] Formaggia, L., and S. Perotto (2003), Anisotropic error estimates for elliptic problems, *Numer. Math.*, *94*(1), 67–92.

[20] Formaggia, L., A. Guadagnini, I. Imperiali, V. Lever, G. Porta, M. Riva, A. Scotti, and L. Tamellini (2013), Global sensitivity analysis through polynomial chaos expansion of a basin-scale geochemical compaction model, *Comput. Geosci.*, *17*(1), 25–42.

[21] Gedeon, M., and D. Mallants (2012), Sensitivity analysis of a combined groundwater flow and solute transport model using local-grid refinement: A case study, *Math. Geosci.*, *44*(7), 881–899.

[22] Gerritsen, M., and J. Lambers (2008), Integration of local–global upscaling and grid adaptivity for simulation of subsurface flow in heterogeneous formations, *Comput. Geosci.*, *12*(2), 193–208.

[23] Haggerty, R., S. A. McKenna, and L. C. Meigs (2000), On the late-time behavior of tracer test breakthrough curves, *Water Resour. Res.*, *36*(12), 3467–3479.

[24] Hecht, F. (2012), New development in Freefem++, *J. Numer. Math.*, *20*(3-4), 251–266.

[25] Huang, W., and X. Zhan (2005), Adaptive moving mesh modeling for two dimensional groundwater flow and transport, *AMS Contemp. Math.*, *383*, 239–252.

[26] Kavetski, D., P. Binning, and S. W. Sloan (2002), Adaptive backward Euler time stepping with truncation error control for numerical modelling of unsaturated fluid flow, *Int. J. Numer. Meth. Engng.*, *53*(6).

[27] Knupp, P. (1996), A moving mesh algorithm for 3-d regional groundwater flow with water table and seepage face, *Adv. Water Res.*, *19*(2), 83–95.

[28] Lagarias, J. C., J. A. Reeds, M. H. Wright, and P. E. Wright (1998), Convergence properties of the Nelder–Mead simplex method in low dimensions, *SIAM J. Optim.*, *9*(1), 112–147.

[29] Levy, M., and B. Berkowitz (2003), Measurement and analysis of non-Fickian dispersion in heterogeneous porous media, *J. Contam. Hydrol.* , *64*(3), 203–226.

[30] Lions, J.L., and E. Magenes (1972), *Non Homogeneous Boundary Value Problems and Applications*, Springer Berlin.

[31] Mansell, R., L. Ma, L. Ahuja, and S. Bloom (2002), Adaptive grid refinement in numerical models for water flow and chemical transport in soil, *Vadose Zone J.*, *1*(2), 222–238.

[32] Masud, A., and T. J. Hughes (2002), A stabilized mixed finite element method for Darcy flow, *Comput. Methods Appl. Mech. Engrg.*, *191*(39), 4341–4370.

[33] Mehl, S., and M. C. Hill (2002), Development and evaluation of a local grid refinement method for block-centered finite-difference groundwater models using shared nodes, *Adv. Water Res.*, *25*(5), 497–511.

[34] Micheletti, S., and S. Perotto (2008), Anisotropic mesh adaption for time-dependent problems, *Int. J. Numer. Meth. Fluids*, *58*(9), 1009–1015.

[35] Micheletti, S., and S. Perotto (2010), Space-time adaptation for purely diffusive problems in an anisotropic framework, *Int. J. Numer. Anal. Model*, *7*(1), 125–155.

[36] Micheletti, S., and S. Perotto (2010), Anisotropic adaptation via a Zienkiewicz–Zhu error estimator for 2d elliptic problems, in *Numerical Mathematics and Advanced Applications 2009*, 645–653.

[37] Micheletti, S., S. Perotto, and P. Farrell (2010), A recovery-based error estimator for anisotropic mesh adaptation in CFD, *SeMA J.*, *50*(1), 115–137.

[38] Mu, L., and R. Jari (2013), A recovery-based error estimate for nonconforming finite volume methods of interface problems, *Appl. Math. Comput.*, *220*, 63–74.

[39] Nassar, M. K., and T. R. Ginn (2014), Impact of numerical artifact of the forward model in the inverse solution of density-dependent flow problem, *Water Resour. Res.*, in press.

[40] Palacios, F., K. Duraisamy, J. J. Alonso, and E. Zuazua (2012), Robust grid adaptation for efficient uncertainty quantification, *AIAA J*, *50*(7), 1538–1546.

[41] Pepper, D., and D. Stephenson (1995), An adaptive finite-element model for calculating subsurface transport of contaminant, *Groundwater*, *33*(3), 486–496.

[42] Pepper, D. W., Y.-t. Chen, and L. Li (1999), Subsurface transport modeling using adaptive finite elements, Water Pollution 99, 5th Int. Conf. on Water Pollution: Modeling, Measuring, and Prediction.

[43] Porta, G., S. Perotto, and F. Ballio (2012), Anisotropic mesh adaptation driven by a recovery-based error estimator for shallow water flow modeling, *Int. J. Numer. Meth. Fluids*, *70*(3), 269–299.

[44] Porta, G., S. Perotto, and F. Ballio (2012), A space–time adaptation scheme for unsteady shallow water problems, *Math. Comput. Simulation*, *82*(12), 2929–2950.

[45] Porta, G., S. Chaynikov, M. Riva, and A. Guadagnini (2013), Upscaling solute transport in porous media from the pore scale to dual-and multicontinuum formulations, *Water Resour. Res.*, *49*(4), 2025–2039.

[46] Quarteroni, A., R. Sacco, and F. Saleri (2007), *Numerical Mathematics*, vol. 37, Springer.

[47] Saaltink, M. W., J. Carrera, and S. Olivella (2004), Mass balance errors when solving the convective form of the transport equation in transient flow problems, *Water Resour. Res.*, *40*(5).

[48] Schmich, M., and B. Vexler (2008), Adaptivity with dynamic meshes for space-time finite element discretizations of parabolic equations, *SIAM J. Sci. Comput.*, *30*(1), 369–393.

[49] Soboĺ, I. M. (2001), Global sensitivity indices for nonlinear mathematical models and their Monte Carlo estimates, *Math. Comput. Simulation*, *55*(1-3), 271–280.

[50] Sudret, B. (2008), Global sensitivity analysis using polynomial chaos expansions, *Reliab. Eng. Syst. Safe.*, *93*(7), 964–979.

[51] Sun, S., and M. F. Wheeler (2006), Anisotropic and dynamic mesh adaptation for discontinuous Galerkin methods applied to reactive transport, *Comput. Methods Appl. Mech. Engrg.*, *195*(25), 3382–3405.

[52] Wexler, E. J. (1992), *Analytical solutions for one-, two-, and three-dimensional solute transport in ground-water systems with uniform flow*, US Government Printing Office.

[53] Xiu, D., and G. E. Karniadakis (2003), Modeling uncertainty in flow simulations via generalized polynomial chaos, *J. Comput. Phys.*, *187*(1), 137–167.

[54] Yan, N. (2001), A posteriori error estimators of gradient recovery type for elliptic obstacle problems, *Adv. Comput. Math.*, *15*(1-4), 333–361.

[55] Younes, A., and P. Ackerer (2005), Solving the advection-diffusion equation with the Eulerian–Lagrangian localized adjoint method on unstructured meshes and non uniform time stepping, *J. Comput. Phys.*, *208*(1), 384–402.

[56] Younes, A., and P. Ackerer (2010), Empirical versus time stepping with embedded error control for density-driven flow in porous media, *Water Resour. Res.*, *46*(8).

[57] Zhang, Y., D. A. Benson, and D. M. Reeves (2009), Time and space nonlocalities underlying fractional-derivative models: Distinction and literature review of field applications, *Adv. Water Res.*, *32*(4), 561–581.

[58] Zienkiewicz, O. C., and J. Z. Zhu (1987), A simple error estimator and adaptive procedure for practical engineerng analysis, *Int. J. Numer. Meth. Engng.*, *24*(2), 337–357.

[59] Zienkiewicz, O. C., and J. Z. Zhu (1992), The superconvergent patch recovery and a posteriori error estimates. Part 1: The recovery technique, *Int. J. Numer. Meth. Engng.*, *33*(7), 1331–1364.

[60] Zienkiewicz, O. C., and J. Z. Zhu (1992), The superconvergent patch recovery and a posteriori error estimates. Part 2: Error estimates and adaptivity, *Int. J. Numer. Meth. Engng.*, *33*(7), 1365–1382.

MOX Technical Reports, last issues

Dipartimento di Matematica "F. Brioschi",
Politecnico di Milano, Via Bonardi 9 - 20133 Milano (Italy)

41/2014 Esfandiar, B.; Porta, G.; Perotto, S.; Guadagnini, A.
Impact of space-time mesh adaptation on solute transport modeling in porous media

40/2014 Antonietti, P.F.; Mazzieri, I.; Quarteroni, A.
Improving seismic risk protection through mathematical modeling

39/2014 Ghiglietti, A.; Paganoni, A.M.
Statistical inference for functional data based on a generalization of Mahalanobis distance

38/2014 Shen, H.; Truong, Y.; Zanini, P.
Independent Component Analysis for Spatial Stochastic Processes on a Lattice

37/2014 Giuliani, N.; Mola, A.; Heltai, L.; Formaggia,L.
FEM SUPG stabilisation of mixed isoparametric BEMs: application to linearised free surface flows

36/2014 Abb,A.;Bonaventura,L.; Nini, M.;Restelli,M.;
Anisotropic dynamic models for Large Eddy Simulation of compressible flows with a high order DG method

35/2014 Tricerri, P.; Dede', L.; Deparis, S.; Quarteroni, A.; Robertson, A.M.; Sequeira, A.
Fluid-structure interaction simulations of cerebral arteries modeled by isotropic and anisotropic constitutive laws

34/2014 Antonietti, P.F.; Pacciarini, P.; Quarteroni, A.
A discontinuous Galerkin Reduced Basis Element method for elliptic problems

33/2014 Canuto, C.; Simoncini, V.; Verani, M.
Contraction and optimality properties of an adaptive Legendre-Galerkin method: the multi-dimensional case

32/2014 Agosti, A.; Formaggia, L.;Scotti, A.
Analysis of a model for precipitation and dissolution coupled with a Darcy flux